

# Synthesis and Growth of Green Graphene from Biochar Revealed by Magnetic Properties of Iron Catalyst

Amel C. Ghogia,<sup>[a]</sup> Lina M. Romero Millán,<sup>[a]</sup> Claire E. White,<sup>[b, d]</sup> and Ange Nzihou<sup>\*[a, c, d]</sup>

Understanding the mechanism of iron-catalyzed graphitization of biomass is an important step for the large-scale synthesis of green graphene. Although iron is known to be the most active transition metal for the catalytic graphitization of cellulose-derived biochar, the direct effect of the iron molecular structure on the formation of highly graphitic carbon remains elusive. Here, biochar was produced from pyrolysis of iron-impregnated cellulose at three different temperatures (1000, 1400, and

1800 °C). X-ray diffraction, X-ray photoelectron spectroscopy, and magnetic measurements were used to probe changes in biochar nanostructure catalyzed by the inclusion of iron. An increase of pyrolysis temperature led to an increase in the iron particle size and the degree of iron reduction, as well as the formation of larger graphitic carbon crystallite sizes, and these two attributes of iron were seen to positively affect the biochar graphitization usually challenging under 2000 °C.

## Introduction

The production of highly graphitic carbon from bioresources represents a major challenge facing sustainable synthesis of graphene.<sup>[1]</sup> This two-dimensional (2D) material made up of a single layer of carbon atoms organized in a hexagonal lattice exhibits high electron mobility ( $250000 \text{ cm}^2 \text{ V}^{-1} \text{ s}^{-1}$ ), outstanding mechanical strength (Young modulus  $E \approx 1 \text{ TPa}$ ), large specific surface area ( $> 2500 \text{ m}^2 \text{ g}^{-1}$ ), and high light transmittance ( $\approx 97.7\%$ ).<sup>[2,3]</sup> Therefore, graphene is considered as a promising material for the development of new technologies in the fields of electronics, supercapacitors, medical devices, and energy storage.<sup>[4]</sup> Both top-down and the bottom-up techniques are currently used to synthesize graphene, where the controlled development of graphene sheets is crucial for attainment of the desired electrical, optical, and mechanical properties.<sup>[5]</sup> In this context, the bottom-up approach offers several advantages in

comparison with top-down, since molecules are built from discrete atomic or small molecular entities, and the fabrication can be carried out with atomic-level precision using synthetic chemical techniques.<sup>[6]</sup> In the bottom-up approach, chemical vapor deposition (CVD) and the thermochemical conversion of biomass under an inert environment are widely used to generate highly graphitic carbon necessary for the production of graphene. The drawback of the CVD technique is that generally, graphitic materials are produced from petroleum-based sources, such as acetylene and methane, which are non-sustainable.<sup>[7,8]</sup>

Biomass precursors, which are complex mixtures of cellulose, hemicellulose, lignin, and inorganic elements, can be used as alternative sources to synthesize highly graphitic carbon.<sup>[9]</sup> However, cellulose, the most abundant source of sustainable carbon, is a non-graphitizable material and may exhibit a randomly oriented carbon nanostructure even after pyrolysis at temperatures higher than 2000 °C.<sup>[10]</sup> Nevertheless, it has been demonstrated that iron-catalyzed graphitization of biomass produces highly graphitic biochar at temperatures lower than 1000 °C, and thus the presence of a catalyst offers an exciting pathway for tuning the properties of graphene at the atomic and molecular level.<sup>[8,11]</sup> Compared to other transition metals commonly used for catalytic graphitization, iron is abundant, non-toxic to the environment, and exhibits superior activity in the graphitization of biomass.<sup>[11–13]</sup> However, few investigations have studied the detailed mechanism of iron-catalyzed graphitization of biomass taking into account the evolution of the catalyst molecular structure and its effect on the emergence of highly graphitic carbon.<sup>[13–16]</sup> The latter constitutes a key step towards large-scale and sustainable synthesis of graphene for a wide range of applications.<sup>[13]</sup>


For iron-based catalysts, the carbon dissolution–graphite precipitation mechanism has been used to explain the formation of graphite-like nanostructures during catalytic graphitization. In this process, the close contact between iron particle and amorphous carbon provides ideal conditions for the nucleation of carbon species from iron particle and


[a] Dr. A. C. Ghogia, Dr. L. M. Romero Millán, Prof. A. Nzihou  
Université de Toulouse, IMT Mines Albi  
UMR CNRS 5302, Centre RAPSODEE  
Campus Jarlard, F-81013 Albi, cedex 09 (France)  
E-mail: ange.nzihou@mines-albi.fr

[b] Prof. C. E. White  
Department of Civil and Environmental Engineering  
Princeton University  
Princeton, NJ 08544 (USA)

[c] Prof. A. Nzihou  
School of Engineering and Applied Science  
Princeton University  
Princeton, NJ 08544 (USA)  
E-mail: ange.nzihou@princeton.edu

[d] Prof. C. E. White, Prof. A. Nzihou  
Andlinger Center for Energy and the Environment  
Princeton University  
Princeton, NJ 08544 (USA)

 Supporting information for this article is available on the WWW under <https://doi.org/10.1002/cssc.202201864>

 © 2022 The Authors. ChemSusChem published by Wiley-VCH GmbH. This is an open access article under the terms of the Creative Commons Attribution Non-Commercial NoDerivs License, which permits use and distribution in any medium, provided the original work is properly cited, the use is non-commercial and no modifications or adaptations are made.

consequently the graphitization of biochar by iron.<sup>[17]</sup> Several studies have shown that the principal identified parameters influencing the catalytic graphitization are reaction temperature, metal precursors, metal loading, metal reduction, and metal particle size and distribution.<sup>[11,15,18]</sup> Neeli and Ramsurn synthesized iron nanoparticles encapsulated by carbon using cellulose, hemicellulose, and lignin. For the three model biomass compounds, the iron core was found to contain mostly  $\alpha$ -Fe (bcc-Fe), orthorhombic  $\text{Fe}_3\text{C}$ , and  $\gamma$ -Fe (fcc-Fe) phases, and the iron particles ranged from 40 to 80 nm.<sup>[15]</sup> However, the direct effect of the iron catalyst molecular structure on the formation of highly graphitic carbon of these model biomass compounds has not been investigated. Recently, Gomez-Martin et al. showed that the formation/decomposition of a  $\text{Fe}_3\text{C}$  phase plays a pivotal role in the graphitization hard carbon at lower temperatures ( $<800^\circ\text{C}$ ) by combining in-situ X-ray diffraction (XRD) and ex-situ total scattering experiments.<sup>[14]</sup> While the atomic iron concentration, metal reduction, and particle size are seen to be important for the formation and the growth of graphene sheets in the biochar matrix, the mechanism by which iron causes the formation of graphene sheets is not yet clearly established.

In this work, we provide new mechanistic insight explaining iron-based catalytic graphitization of cellulose. To this end, our experimental approach based on XRD, X-ray photoelectron spectroscopy (XPS), and magnetic measurements used to determine graphite and iron crystallite sizes and the reduction degree of iron during the pyrolysis at different temperatures. From these data we proposed that during catalytic graphitization, the reduction of iron oxide by CO into metallic iron start first at low temperature. Then, an increase in temperature promotes the formation of a broad population of particles composed of small and large particles resulting from thermal sintering. The highest degree of reduction for the largest particles leads to the highest number of stacked layers.

## Results and Discussion

### Trends on crystallite size of carbon and iron particles

The carbon crystallite size (i.e., size of ordered graphitic domains) is widely used to describe the nanostructure of carbon materials (see Experimental Section).<sup>[2,19]</sup> The crystallite size parameters include the height of the organized stacking of graphene sheets  $L_c$  and the lateral extension of the graphene sheets  $L_a$ , while  $d_{002}$  denotes the average spacing between these sheets. Graphitization of a carbon source, such as the biochar matrix of the samples in this investigation, will lead to an increase of the carbon crystallite size. XRD has been used extensively in the past to characterize the nanostructure of carbon materials and determine apparent crystallite dimensions.<sup>[20]</sup> As presented in the Experimental Section, the  $L_c$  and  $L_a$  crystallite parameters can be deduced using the Debye–Scherrer equation, while the  $d_{002}$  distance can be calculated from Bragg's law. It should be mentioned that in this work, the crystallite size calculation was performed only for low ash-

content samples (i.e., pyrolyzed crystalline cellulose), since the presence of inorganic species in the cellulose can misguide the analysis of the graphite Bragg peaks.<sup>[21]</sup> The XRD results obtained for the iron-impregnated biochar are presented in Figure 1a. Analysis of these data confirms the positive effect that the pyrolysis temperature has on the graphitization of biochar. It can be observed from Figure 1a that the (002) carbon Bragg peak sharpens with increasing pyrolysis temperature. In addition, from 1000 to 1800 °C the average crystallite size of the samples increases from 4.7 to 6.4 nm for  $L_c$ , and from 5.4 to 7.2 nm for  $L_a$  (Figure 1b). This confirms the impact of both temperature in enhancing the graphitization of biochar during pyrolysis.<sup>[14,19]</sup> The Debye–Scherrer equation (see Experimental Section) can also be used to deduce the iron particle size, which is found to be 21 nm after heating to 1000 °C, 25 nm for 1400 °C, and 31 nm for 1800 °C. In this case, the increase in pyrolysis temperature provokes agglomeration and sintering of the iron particles, and hence an increase of their size.<sup>[19]</sup> A similar trend was observed by Hoekstra et al. for iron-catalyzed graphitization of carbonized cellulose.<sup>[19]</sup>

The atomic arrangements and variations in the nanostructure of graphene sheets have a drastic influence on their unique properties.<sup>[22]</sup> Therefore, high-resolution transmission electron microscopy (HRTEM) is a useful technique to assess the graphitization of the carbon matrix during pyrolysis. HRTEM

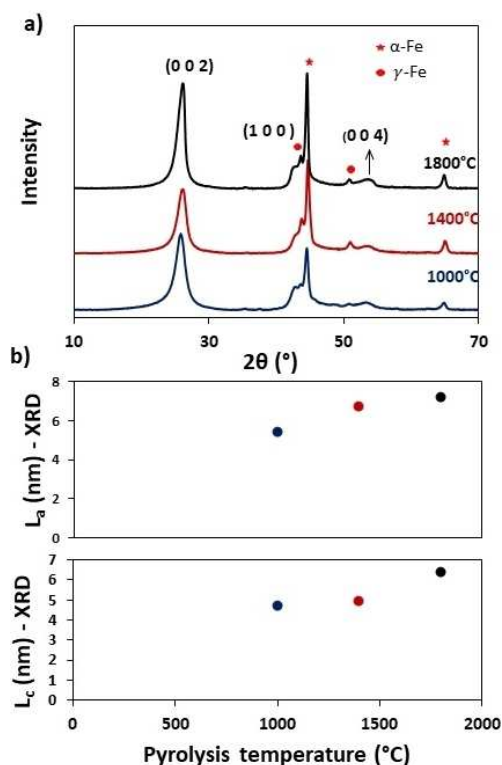


**Figure 1.** XRD patterns of graphitic biochar pyrolyzed at 1000, 1400, and 1800 °C. (a) Highly graphitic biochar from iron-impregnated cellulose. \*  $\alpha$ -Fe (ferrite), ●  $\gamma$ -Fe (austenite), and indices (002), (100), and (004) are noted for the carbon peaks based on the crystal structure of graphite. (b) Evolution of the carbon crystallite size with the pyrolysis temperature. The values of the carbon crystallite size were calculated from XRD patterns.

images of the graphitic biochar pyrolyzed at 1000, 1400, and 1800 °C are presented in Figure 2a–j. TEM images show highly crystalline graphitic domains, creating long-range stacked carbon layers (Figure 2a,b,d,e,g,h), which could explain the increase in the average crystallite sizes  $L_a$  and  $L_c$  as shown by XRD (Figure 1b). This was confirmed by selected area electron diffraction (SAED) analyses, which show the appearance of diffraction spots, indicating the presence of an ordered crystalline graphitic structure.<sup>[23]</sup> The location of the diffuse ring at around  $9.18 \text{ nm}^{-1}$  corresponds to a  $d$ -spacing of 0.204 nm for the (101) reflection. These observations are in agreement with XRD analyses.

### Iron reduction degree and particle size distribution

Apart from the iron particle size, additional parameters such as degree of iron reduction and particle size distribution can also be used to rationalize the effects of the iron catalyst on graphitization of biochar.<sup>[18]</sup> Indeed, during the catalytic graphitization of biochar, a gradual increase in temperature under a CO reducing atmosphere (CO resulting from the decomposition of cellulose) will lead to a modification of the degree of iron reduction and the particle size. The change in the particle size and the degree of reduction will have a direct impact on the magnetic properties of iron, specifically the saturation magnetization ( $M_s$ ), the remanent magnetization ( $M_R$ ), and the coercive field ( $H_c$ ). The saturation magnetization is linked to the degree of iron reduction<sup>[19]</sup> while the remanent magnetization and the

coercive field are related to the particle size.<sup>[24]</sup> Here, a vibrating-sample magnetometer (VSM) was used to access these magnetic properties of iron after pyrolysis of iron-impregnated biochar, where the measurements were performed at room temperature.<sup>[25]</sup> Figure 3a,b shows the magnetic hysteresis loop for the different samples recorded at 300 K. The saturation magnetization ( $M_s$ ) for the samples pyrolyzed at 1000, 1400, and 1800 °C is 87, 90, and 100  $\text{emu g}_{\text{Fe}}^{-1}$ , respectively. These values are lower than the saturation magnetization of bulk iron ( $212 \text{ emu g}_{\text{Fe}}^{-1}$ ).<sup>[19]</sup> This can be attributed to the partial oxidation of iron particles after exposure to air and may also explain this low saturation magnetization per unit mass.<sup>[19]</sup> It can be observed from the TEM images in Figure 3f that the iron particles are not completely encapsulated within sheets of graphitic biochar. Based on the saturation magnetization of each sample and considering the magnetization of bulk iron, the reduction degree was evaluated to be 41 % for 1000 °C, 43 % for 1400 °C, and 47 % for 1800 °C. The sample at 1800 °C has the highest reduction degree (47%). This is not surprising considering that the reduction of iron oxide, promoted by carboreduction, is enhanced at high temperature from the thermodynamic point of view.

As shown by XRD analysis, the increase in temperature results in an increase of iron particle size due to thermal sintering (Figure 3c). It has been reported that a change in particle size of a metal strongly affects the coercive field and the remanent magnetization.<sup>[26]</sup> Specifically, analysis of these two magnetic parameters can provide insight on how a change in particle size can be accompanied by the transition between predominantly mono-domain particles to those consisting of multi-domains.<sup>[27]</sup> Figure 3c shows the influence of pyrolysis temperature on iron particle size and coercive field, where a decrease in the coercive field is observed with increasing pyrolysis temperature. The same trend is also seen for the remanent magnetization (Figure 3d). The decrease in the coercive field and remanent magnetization can be attributed to the size increase of the iron particles, where larger particles contain more crystallites and thus also contain more magnetic domains that are randomly oriented.<sup>[24]</sup> Similar trends of evolution of  $H_c$  and  $M_R$  with particle size have been observed in the literature for the synthesis of  $\text{Fe}_3\text{O}_4$  nanoparticles.<sup>[24]</sup>

Zero-field-cooled (ZFC) and field cooled (FC) magnetization measurements (Figure 4a–c) provide insight on the magnetic characteristics of the iron particles as a function of temperature, where this behavior can be used to estimate the particle size distribution established by pyrolysis. The particle size distribution can be used to control the number of graphene sheets stacked during biochar graphitization, where a change in the size distribution occurs during collision and sintering of iron particles.<sup>[28]</sup> Figure 4a–c shows the ZFC-FC magnetization recorded at  $H = 50 \text{ Oe}$  for the different samples produced at 1000, 1400, and 1800 °C. For the sample at 1000 °C, the ZFC curve increases from 0 to 100 K and then decreases up to 300 K, while for the samples at 1400 and 1800 °C there is a gradual increase in magnetization with temperature. The shape of the ZFC-FC curves shows that the blocking temperature  $T_B$  is beyond 300 K, which can be attributed to the large iron particles due to the

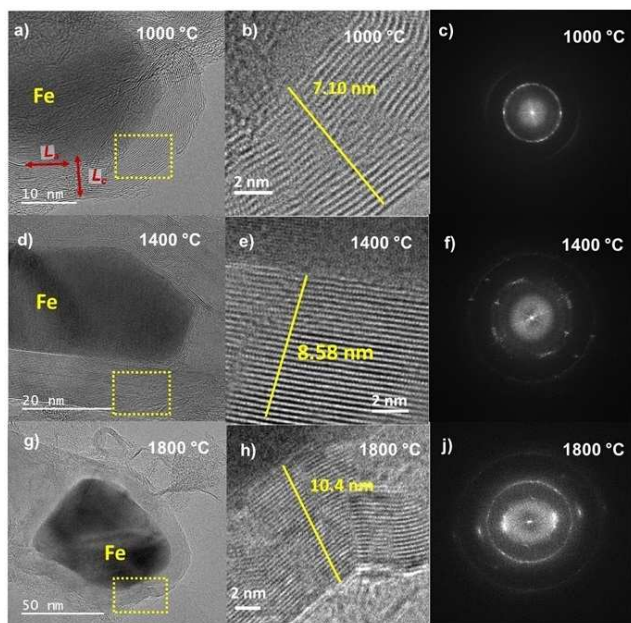


**Figure 2.** HRTEM images and the corresponding SAED of graphitic biochar pyrolyzed at 1000, 1400, and 1800 °C: (a–c) 1000 °C, (d–f) 1400 °C, and (g–j) 1800 °C. The yellow dotted rectangles on the TEM images represent the areas that were used to obtain diffraction patterns. The corresponding diffraction patterns show a diffuse diffraction ring with strong intensity similar to crystal graphite; the yellow line shows the vertical stacking height of the graphene layers.

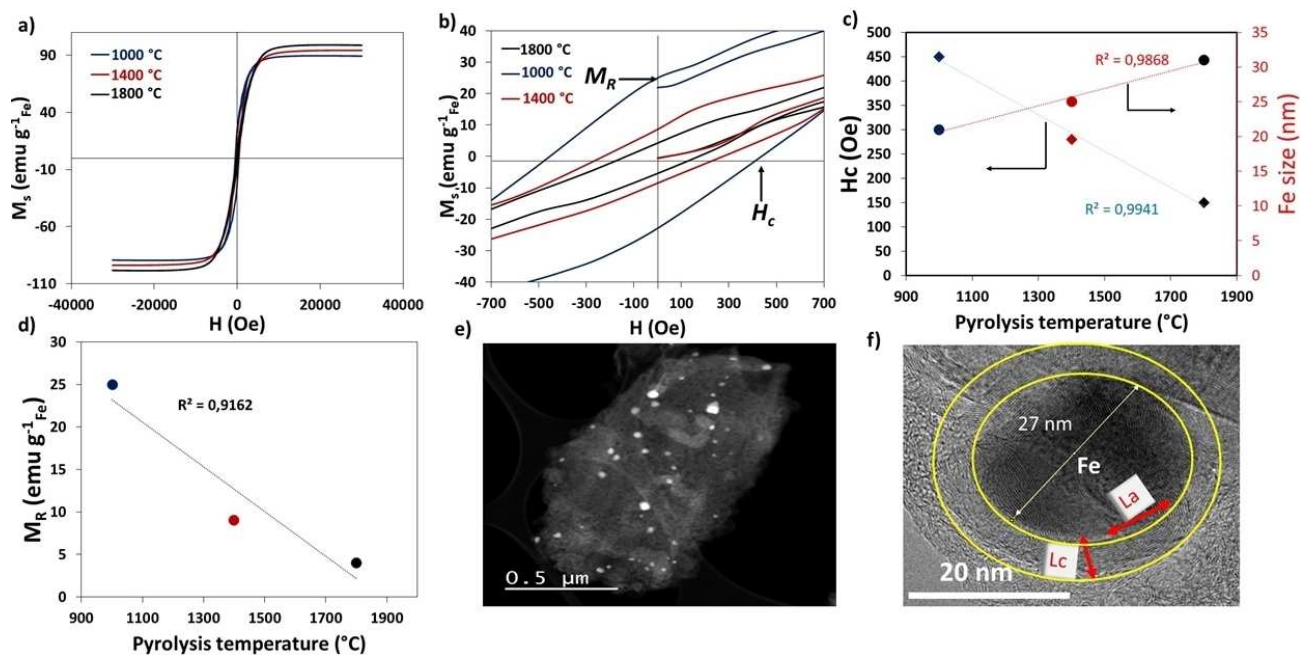


**Figure 3.** Ferromagnetic character of the iron-impregnated biochar pyrolyzed at 1000, 1400, and 1800 °C. (a,b) Magnetization, the remanent magnetization ( $M_R$ ), coercive field ( $H_c$ ) versus magnetic field of the produced biochar obtained at 27 °C (300 K). Influence of pyrolysis temperature on (c) coercive field and iron particle size, and (d) remanent magnetization. TEM images of the produced graphitic biochar pyrolyzed at 1400 °C: (e) low and (f) high resolution showing the long-range stacked graphene sheets around the large iron particle (from the sintering of the small particles).

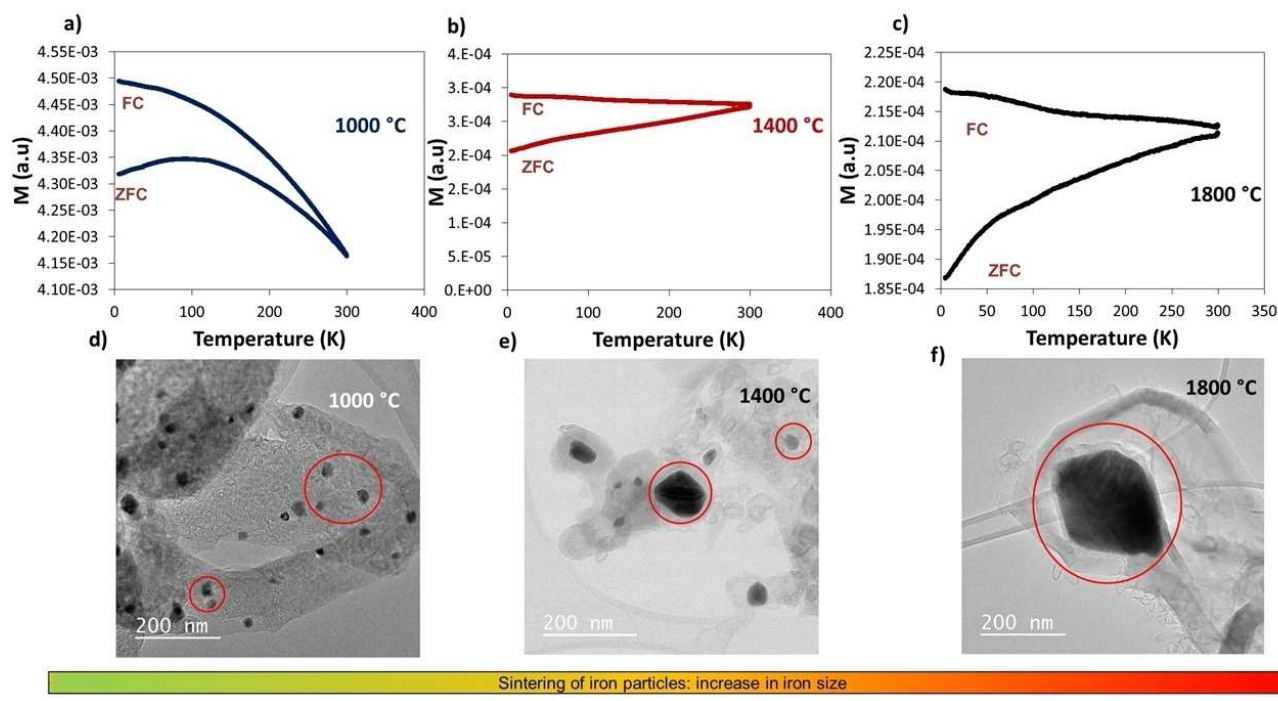


**Figure 4.** ZFC-FC magnetization as a function of temperature recorded at 50 Oe associated with the corresponding TEM images of the graphitic biochar obtained at different temperatures. (a,b) 1000 °C, (c,d) 1400 °C, (e,f) 1800 °C. TEM images show the increase in iron particle size with increasing pyrolysis temperature.

disappearance of small particles induced by the increase in the pyrolysis temperature ( $T > 600$  °C).<sup>[19,29]</sup> In comparison with ZFC curves of samples at 1400 and 1800 °C, the decrease observed

for the sample at 1000 °C from 100 K is due to the relaxation of the spin moments of the smallest particles, which are present in larger quantities, as shown in the TEM images (Figure 4d,f).<sup>[29]</sup>

The splitting of the ZFC and FC magnetization explains the co-existence of a core-shell structure composed of carbon phase (antiferromagnetic) that coats the iron nanoparticles (ferromagnetic).<sup>[29]</sup>

### Iron carbon core-shell particles during pyrolysis

The existence of iron carbon core-shell particles in the pyrolyzed iron-impregnated biochar samples can be explained using the reported carbon dissolution-precipitation mechanism.<sup>[15]</sup> The graphitic layers/shells form when the carbon atoms that are dissolved in a liquid state precipitate as graphene sheets on the surface of the iron particle, where growth of the graphitic structure occurs from these nucleation sites.<sup>[15]</sup> Here, we have used XPS analysis to determine the change in the atomic surface concentration of iron as a means of monitoring the encapsulation of iron particles by graphene sheets during pyrolysis. Figure 5a shows the Fe 2p spectra of the produced graphitic biochars, and the results obtained from deconvolution of these spectra are presented in Table S2.

The atomic contents of Fe 2p and C 1s are also presented (Table S2). The XPS peaks from 2p<sub>3/2</sub> at 710.5–713.7 eV and 2p<sub>1/2</sub> at 723.5–727.9 eV are characteristic of the presence of Fe<sup>3+</sup> and Fe<sup>2+</sup> species. As seen in Figure 4b the Fe/C atomic ratio decreases with increasing pyrolysis temperature. This means that the atomic iron concentration decreases with increasing

temperature from 1000 to 1800 °C, which can be explained by graphitic sheets coating the iron particles rendering the iron inaccessible to XPS analysis (depth probed by XPS: 2–10 nm).<sup>[30]</sup> Furthermore, a good correlation is obtained between the Fe/C ratio and pyrolysis temperature for the samples treated at 1000, 1400, and 1800 °C (Figure 5b). Shi et al. showed that iron carbon core-shell particles begin to form at 800 °C.<sup>[31]</sup> Figure S1 and Table S2 shows that the quantity of C-sp<sup>2</sup> increases with increasing pyrolysis temperature, reflecting the improvement in graphitization at higher temperatures.

### Effects of the iron structure on the catalytic graphitization of biochar

As shown in Figure 6a–f, properties of iron catalyst such as degree of iron reduction, particle size, and atomic iron concentration obtained from magnetic measurements, XRD, and XPS, respectively, can be linked to the L<sub>c</sub> and L<sub>a</sub> crystallite size of graphitic carbon in order to establish correlations between the iron structure and extent of graphitization. As seen in this figure, single parameter correlations with the L<sub>c</sub> and L<sub>a</sub> crystallites size values are obtained, which indicates that the properties of the iron catalyst can be used to explain the graphitization of biochar. Biochar produced at 1800 °C has (i) the largest graphitic crystallite sizes L<sub>c</sub> and L<sub>a</sub>, (ii) the highest degree of iron reduction (47%), (iii) the largest average iron particle size (31 nm), and (iv) the lowest concentration of iron accessible using XPS (see Figure 6a–f).

This means that the increase of degree of iron reduction and average iron particle size positively affect the biochar graphitization. In fact, a high degree of reduction improves the reactivity of the catalyst due to the increase in the proportion of the iron metallic phase.<sup>[32]</sup> It was reported that carbon atoms start dissolving in the presence of the metallic iron surface of  $\alpha$ -Fe due to the unpaired electron affinity between orbital 2p of carbon and 3d of pure iron.<sup>[15]</sup> For the particle size effect, the dissolution/precipitation of carbon, which results in the formation of the graphitic structure, is more prevalent for large particles than for small ones.<sup>[18]</sup> Large particles graphitize the carbon around them in a more ordered manner due to the larger facets.<sup>[18]</sup> Figure 6e,f shows a good correlation between the iron surface concentration and the L<sub>c</sub> and L<sub>a</sub> crystallite sizes. Obviously, a lower iron surface concentration reflects an improvement in the encapsulation and therefore extent of biochar graphitization.

The most relevant phenomena occurring during graphitization of cellulose-derived biochar are summarized in Scheme 1 with six key steps. The impregnation step disperses the Fe(NO<sub>3</sub>)<sub>3</sub> in the cellulose matrix. The simultaneous decomposition of the iron precursor and the biochar matrix via carbon gasification under the effect of temperature leads to the formation of compounds such as: iron oxide, CO, CO<sub>2</sub>, H<sub>2</sub>, and H<sub>2</sub>O (step 1 and 2).<sup>[15]</sup> Subsequently, the reduction of iron oxide into metallic iron can take place in three pathways as shown in Table S3 (step 3). Based on thermodynamic considerations, biochar gasification (reactions a and b in Table S3), which produces CO

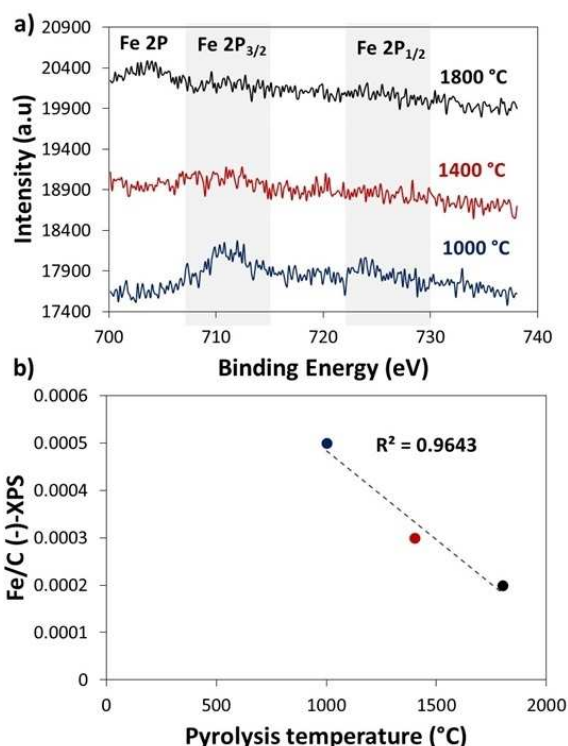


**Figure 5.** XPS spectra of the produced biochar at 1000, 1400, and 1800 °C. (a) Fe 2p XPS spectra of the produced graphitic biochar. (b) Relationship between the Fe/C ratio (atomic iron concentration) and pyrolysis temperature for the samples obtained at 1000, 1400, and 1800 °C.

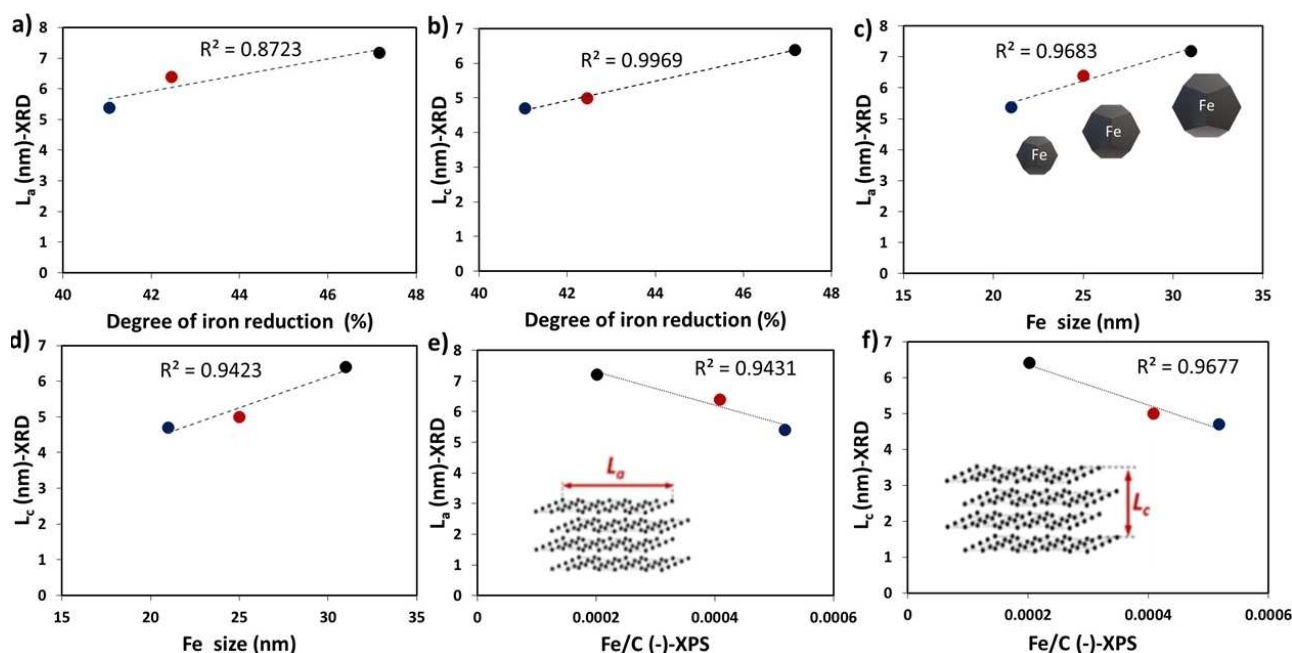
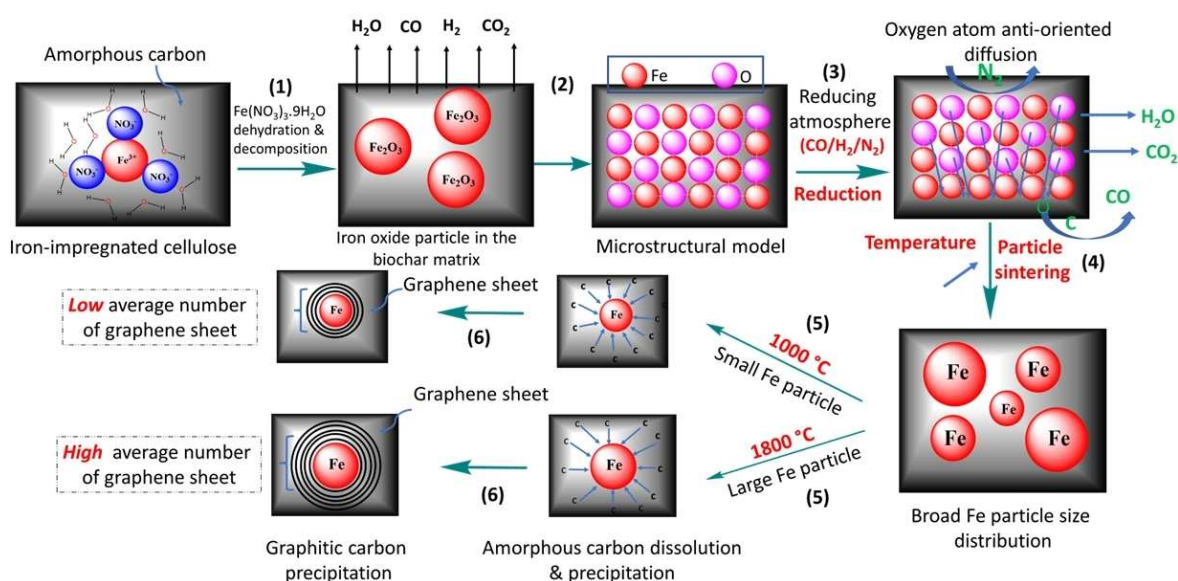


**Figure 6.** Ferromagnetic character and iron particle size of the produced biochar. Degree of iron reduction, iron particle size, and iron surface concentration of iron-impregnated biochar pyrolyzed at 1000, 1400, and 1800 °C. Comparison between single parameter catalyst and crystallite size ( $L_a$  and  $L_c$ ): (a,b) iron reduction degree; (c,d) iron particle size; (e,f) atomic iron concentration (Fe/C).



**Scheme 1.** Most relevant phenomena occurring during graphitization of cellulose-derived biochar. Mechanisms controlling iron-catalyzed graphitization of cellulose-derived biochar.

and  $H_2$ , is favorable at relatively low temperature (Figure 7). Furthermore, the reduction of  $Fe_2O_3$  by CO (reaction d) is thermodynamically more favorable at lower temperature than the reduction with carbon material and by  $H_2$  (reactions c and e, respectively).<sup>[15]</sup> In fact the reduction of  $Fe_2O_3$  by CO is an exothermic reaction at room temperature and occurs at low temperature. Then, an increase in temperature promotes the formation of a broad population of particles composed of small

and large particles resulting from thermal sintering due to random rearrangement of particles (step 4).<sup>[33]</sup> The carbon atoms resulting from the decomposition of the biochar matrix partially dissolve into the liquid state (step 5) and precipitate as graphene sheets on the surface of the metallic iron particles (step 6). The encapsulation of the iron particle by a single- or multi-graphitic sheet occurs during the nucleation and growth of the carbon species.<sup>[34]</sup> The degree of iron reduction being

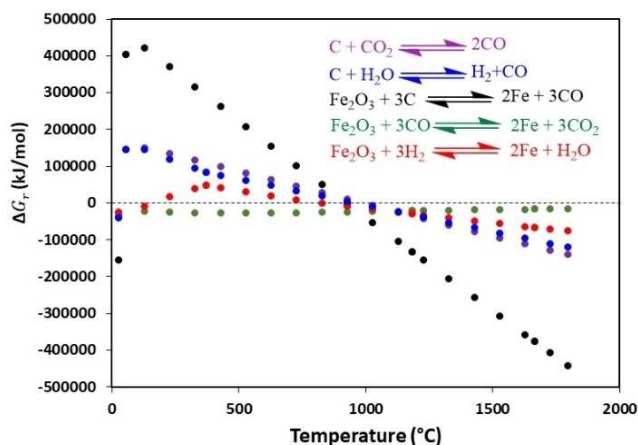


**Figure 7.** Evolution of Gibbs free energy reaction as a function of reaction temperature (50–1800 °C) at 1 atm. The Gibbs free energy reaction was calculated using FactSage software.

highest for the largest particles, which leads to the highest number of stacked layers. As such, large iron particles thermodynamically favor graphitic encapsulation.<sup>[34]</sup>

Both the graphitization of carbon-rich iron amorphous mixture and the graphitic encapsulation of iron were observed in the literature for iron carbide and catalytic carbon nanotube production.<sup>[25,26]</sup> This study has evidenced similar mechanisms for complex polymeric carbon from bioresource such as cellulose, and should pave a way for future research in the field.

## Conclusion

Highly graphitic biochar has been generated by pyrolysis of iron-impregnated cellulose at 1000, 1400, and 1800 °C. The effect of the structure of iron catalyst on biochar graphitization has been investigated by combining magnetic measurements, X-ray photoelectron spectroscopy, and X-ray diffraction. From these new findings a comprehensive graphitization mechanism is proposed that takes into account the unique behavior of the iron catalyst and evolution of the carbon structure during the graphitization process. Our results show that the graphitic carbon crystallite size increases with processing temperature, and the highest processing temperature of 1800 °C is correlated with large metallic iron particles possessing a relatively broad distribution of sizes that are in the most reduced state. This suggests that both particle size and degree of reduction of the iron catalyst positively impacts biochar graphitization, and in particular the large facets of the bigger iron particles provide regions for precipitation of graphitic carbon, where precipitation is promoted by the reduced nature of the metallic iron. Moreover, the metallic iron reduces the barrier for carbon nucleation and makes it easier for graphite to form. Encapsulation of iron particles by graphene sheets is more pronounced for large particles, which are prevalent at higher temperatures due to more extensive sintering. These results show that the key parameters of the structure of iron catalyst play a pivotal

role in biochar graphitization. This comprehensive mechanism of biochar graphitization serves as a breakthrough contribution to the literature in the field of the synthesis of graphene-like materials from hard carbon such as cellulose that is extremely challenging to graphitize.

## Experimental Section

### Impregnation procedure and determination of chemical composition

Microcrystalline cellulose [Sigma Aldrich, CEL] was used in this study to analyze the graphitization behavior of cellulose-derived biochar. Microcrystalline cellulose was impregnated with an iron nitrate solution prepared with  $\text{Fe}(\text{NO}_3)_3 \cdot 9\text{H}_2\text{O}$  (Sigma Aldrich, 99% purity). 20 g of each sample was immersed in 200 mL of a 0.049 M solution under continuous stirring for 6 h. The samples were then filtered and dried at 105 °C for 24 h. To determine the inorganic composition of the impregnated samples, 50 mg of sample was acid-digested in closed vessels at 220 °C during 4 h. Acid reagents  $\text{H}_2\text{O}_2$ ,  $\text{HNO}_3$ , HF, and  $\text{H}_3\text{BO}_3$  were used according to EN 16967. Acid solutions were diluted with demineralized water to 50 mL and analyzed using a HORIBA Jobin Yvol Ultima 2 inductively coupled plasma optical emission spectrometer (ICP-OES). The CHNS composition of the samples was determined using a Thermoquest NA 2000 elemental analyzer, and their ash content was calculated according to the standard EN ISO 18122. The composition of the non- and iron-impregnated cellulose is summarized in Table S1.

### Graphitization experiments

The pyrolysis of the impregnated cellulose was performed in a horizontal laboratory-scale reactor, with an internal diameter of 20 mm, externally heated with an electric furnace. For each experiment, between 0.5–1 g of sample was placed inside the reactor using a high-temperature ceramic crucible. Impregnated cellulose was heated to 1000, 1400, or 1800 °C with a heating rate of 8 °C min<sup>-1</sup>, under a nitrogen atmosphere with a gas flow of 1000 mL min<sup>-1</sup>. The pyrolysis temperature was maintained for 1 h and then the reactor was cooled down to room temperature. Finally, the resulting biochar was collected, weighed, and stored for further characterization.

### Characterization of graphitic biochar using XRD

XRD analysis was conducted using a Phillips Panalytical X'pert Pro MPD diffractometer and a  $\text{Cu K}_\alpha$  radiation source (1.543 Å) with a voltage of 4 kV and current of 40 mA. The diffraction patterns were collected for powder samples (particle size below 250 μm) between  $2\theta = 10^\circ$  and  $2\theta = 70^\circ$  with a step of 0.05°.

The structure of the biochar samples and the average size of crystallites of the catalyst ( $d_{\text{Fe}}$ ) were determined from analysis of the XRD patterns. Particular attention was given to the width of the carbon bands (002) and (10), which are related to the extent of atomic order of graphite-like carbon in the out-of-plane and in-plane direction, respectively.<sup>[35]</sup> The characteristic peak of  $\alpha$ -Fe located at  $2\theta = 44.5^\circ$  was used in the Scherrer equation to determine the crystallite size of the catalyst. To determine the carbon structural parameters and the crystallite size of the catalyst, the (002) and (10) bands, and the peak located at  $2\theta = 44.5^\circ$  were fitted with HighScore software, using pseudo-Voigt functions. The instrument broadening in XRD analysis was removed in order to

have accurate values of the  $L_c$  and  $L_a$  parameters, and  $d_{Fe}$ . Thus, a standard NIST sample (silicon) was analyzed under the same conditions as those of the samples. The pseudo-Voigt functions were also used for standard peaks fitting. Since the Voigt function is a convolution of Gaussian and Lorentzian functions, and that the Lorentzian function is the dominant cause of broadening,<sup>[36]</sup> the correction of the mid-width was performed using Lorentzian shape [see Eq. (1)].

The sample and standard peaks width at the half-maximum was automatically calculated by the software, and these values were used to calculate the corrected peak width [Eq. (1)]. Then, this latter was used to calculate the average carbon crystallite domain size and the average size of crystallites of the catalyst.

$$\beta_{size} = \beta_{obs} - \beta_{inst} \quad (1)$$

Here,  $\beta_{size}$  is the corrected peak width at the half-maximum intensity in radians,  $\beta_{obs}$  is the sample peak width at the half-maximum intensity in radians, and  $\beta_{inst}$  is the peak width from instrument broadening at the half-maximum intensity in radians.

Accordingly, the average crystallite size  $L$  of the samples, the average distance between carbon layers  $d_{002}$ , and the average size of crystallites of the catalyst  $d_{Fe}$  were expressed by the Debye-Scherrer equation [Eq. (2)] and Bragg's law [Eq. (3)], and the Debye-Scherrer equation [Eq. (4)], respectively:

$$L = \frac{K\lambda}{\beta_{size} \cos\theta} \quad (2)$$

$$d_{002} = \frac{\lambda}{2\sin\theta_{002}} \quad (3)$$

$$d_{Fe} = \frac{K'\lambda}{\beta_{size} \cos\theta} \quad (4)$$

where  $\theta$  is the peak position in radians,  $\lambda$  is the X-ray wavelength in nm, and  $K$  is a constant that generally depends on the shape of the crystallite.<sup>[37]</sup> The calculations were performed with  $K$  values of 0.89 for  $L_c$  (graphitic planes stacking in the carbon crystallite), and 1.84 for  $L_a$  (graphite-like atomic order in the single plane).<sup>[38]</sup>  $K'$  value is 0.94 for  $d_{Fe}$ .

### Characterization of graphitic biochar using HRTEM

The structure of the prepared biochar was observed using a JEOL JEM-ARM200F HRTEM. Powder samples with particle sizes below 250  $\mu\text{m}$  were dispersed in ethanol and mixed in an ultrasonic bath. The samples were then collected from the surface of the solution and deposited onto carbon support films before analysis.

### Characterization of graphitic biochar using magnetic measurements

Magnetic measurements were carried out at 300 K and field up to 30000 Oe using a Quantum Design Vibrating Sample Magnetometer (VSM).<sup>[30]</sup> This measurement allows to determine the saturation magnetization [ $M_s$ , Eq. (5)] of biochar containing iron under the effect of a magnetic field and to deduce the degree of reduction [Eq. (6)] of the iron catalyst after pyrolysis knowing the saturation magnetization of the bulk iron ( $M_s$  bulk, equal to 212  $\text{emu g}_{Fe}^{-1}$ ).

$$M_s \text{ biochar} [\text{emu g}_{Fe}^{-1}] = \frac{M_s(\text{VSM})}{m_{bio} \times \%Fe} \quad (5)$$

with  $M_s$  (VSM) the magnetization obtained by the VSM at room temperature,  $m_{bio}$  the mass of the biochar, and %Fe the iron content obtained by ICP.

$$\text{Degree of reduction} [\%] = \frac{M_s \text{ biochar}}{M_s \text{ bulk}} \quad (6)$$

The VSM measurements were performed on biochar after air exposure. VSM capsules were filled with 5–10 mg of biochar and sealed. The capsule containing biochar was introduced into the equipment. A hysteresis cycle was performed at 300 K and the field-dependent magnetization was recorded. For ZFC-FC measurements, magnetization curves were recorded at 0 K first after a (ZFC) and second after a (FC) from 300 K down to 0 K under 50 Oe.<sup>[39]</sup>

### Characterization of graphitic biochar using XPS

Analysis was investigated using a monochromatized Al  $K_{\alpha}$  source on a ThermoScientific  $K_{\alpha}$ .<sup>[30]</sup> The X-ray spot size varies from 30 to 400  $\mu\text{m}$ . The pass energy was fixed at 30 eV with a step of 0.1 eV for core levels and 160 eV for surveys (step 1 eV).<sup>[30]</sup> Energy calibration of the spectrometer was performed using the Cu  $2p_{3/2}$  ( $932.8 \pm 0.1$  eV) and Au  $4f_{7/2}$  ( $83.9 \pm 0.1$  eV) photoelectron lines. Spectra were recorded in direct mode and the background signal was removed using the Shirley method.<sup>[40]</sup>

### Acknowledgements

The authors thanks colleagues at RAPSODEE Center- IMT Mines Albi (N. Lyczko), Centre de MicroCaractérisation Raimond Castaing (T. Hungria), LPCNO (G. Ballon). This work is supported by the French "Investissements d'Avenir" program under the Laboratory of Excellence, LABEX SOLSTICE, ANR-10-LABX-22-01 grant. This work was also financial supported by the Fulbright Commission in granting Professor Nzihou with a research scholarship at Princeton University.

### Conflict of Interest

The authors declare no conflict of interest.

### Data Availability Statement

The data that support the findings of this study are available in the supplementary material of this article.

**Keywords:** carbon materials · encapsulation · graphitic biochar · iron · particle size

[1] Q. Chen, X. Tan, Y. Liu, S. Liu, M. Li, Y. Gu, P. Zhang, S. Ye, Z. Yang, Y. Yang, *J. Mater. Chem.* **2020**, *8*, 5773–5811.



- [2] M. Inagaki, F. Kang, M. Toyoda, H. Konno, *Advanced Materials Science and Engineering of Carbon*, Elsevier Inc., **2014**.
- [3] Y. Zhu, S. Murali, W. Cai, X. Li, J. W. Suk, J. R. Potts, R. S. Ruoff, *Adv. Mater.* **2010**, *22*, 3906–3924.
- [4] S. Ren, P. Rong, Q. Yu, *Ceram. Int.* **2018**, *44*, 11940–11955.
- [5] S. C. Joffrey Pijeat, Jean-Sébastien Lauret, in *Graphene Nanoribbons*, **2019**, p. 11.
- [6] J. M. Tour, *Chem. Mater.* **2014**, *26*, 163–171.
- [7] G. Synthesis, M. Saeed, Y. Alshammari, S. A. Majeed, *Molecules* **2020**, *25*, 2–62.
- [8] I. Major, J.-M. Pin, E. Behazin, A. Rodriguez-Uribe, M. Misra, A. Mohanty, *Green Chem.* **2018**, *20*, 2269.
- [9] S. Yoo, C.-C. Chung, S. S. Kelley, S. Park, *ACS Sustainable Chem. Eng.* **2018**, *6*, 9113–9119.
- [10] R. Franklin, *Proc. Roy. Soc. A* **1947**, *71*, 196–218.
- [11] L. Gai, J. Li, Q. Wang, R. Tian, K. Li, *J. Environ. Chem. Eng.* **2021**, *9*, 106678.
- [12] J. Hoekstra, A. M. Beale, F. Soulimani, M. Versluijs-Helder, J. W. Geus, L. W. Jenneskens, *J. Phys. Chem.* **2015**, *119*, 10653–10661.
- [13] E. Thompson, A. E. Danks, L. Bourgeois, Z. Schnepf, *Green Chem.* **2015**, *17*, 551.
- [14] A. Gomez-Martin, Z. Schnepf, J. Ramirez-Rico, *Chem. Mater.* **2021**, *33*, 3087–3097.
- [15] S. T. Neeli, H. Ramsurn, *Carbon* **2018**, *134*, 480–490.
- [16] R. D. Hunter, J. Ramirez-Rico, Z. Schnepf, *J. Mater. Chem. A* **2022**, *10*, 4489–4516.
- [17] H. Li, H. Zhang, K. Li, J. Zhang, M. Sun, B. Su, *Fuel* **2020**, *279*, 118531.
- [18] S. J. Goldie, S. Jiang, K. S. Coleman, *Mater Adv* **2021**, *2*, 3353–3361.
- [19] J. Hoekstra, A. M. Beale, F. Soulimani, M. Versluijs-Helder, D. Van De Kleut, J. M. Koelewijn, J. W. Geus, L. W. Jenneskens, *Carbon* **2016**, *107*, 248–260.
- [20] C. F. Holder, R. E. Schaak, *ACS Nano* **2019**, *13*, 7359–7365.
- [21] J. S. Clemente, S. Beauchemin, Y. Thibault, T. Mackinnon, D. Smith, *ACS Omega* **2018**, *3*, 6931–6944.
- [22] J. R. Jinschek, E. Yucelen, H. A. Calderon, B. Freitag, *Carbon* **2011**, *49*, 556–562.
- [23] J. Li, Y. Qin, Y. Chen, Y. Song, Z. Wang, *Carbon* **2021**, *187*, 133–144.
- [24] Q. Li, C. W. Kartikowati, S. Horie, T. Ogi, T. Iwaki, K. Okuyama, *Sci. Rep.* **2017**, *7*, 1–4..
- [25] L. M. Lacroix, N. Frey Huls, D. Ho, X. Sun, K. Cheng, S. Sun, *Nano Lett.* **2011**, *11*, 1641–1645.
- [26] M. P. Fernández-García, P. Gorria, M. Sevilla, M. P. Proena, R. Boada, J. Chaboy, A. B. Fuertes, J. A. Blanco, *J. Phys. Chem.* **2011**, *115*, 5294–5300.
- [27] J. Carvell, E. Ayieta, A. Gavrin, R. Cheng, V. R. Shah, P. Sokol, *J. Appl. Phys.* **2010**, *107*, 103913.
- [28] A. Moisala, A. G. Nasibulin, E. I. Kauppinen, *J. Phys. Condens. Matter* **2003**, *15*, S3011.
- [29] F. Huang, Z. Wang, X. Lu, J. Zhang, K. Min, W. Lin, R. Ti, T. Xu, J. He, C. Yue, J. Zhu, *Sci. Rep.* **2013**, *3*, 1–7..
- [30] A. C. Ghogia, B. F. Machado, S. Cayez, A. Nzihou, P. Serp, K. Soulantica, D. Pham Minh, *J. Catal.* **2021**, *397*, 156–171.
- [31] S. Q. Shi, W. Che, K. Liang, C. Xia, D. Zhang, *J. Anal. Appl. Pyrolysis* **2015**, *115*, 1–6..
- [32] W. Yang, Y. Feng, W. Chu, *J. Nanotechnol.* **2014**, 547030.
- [33] D. V. Dudina, A. V. Ukhina, B. B. Bokhonov, M. A. Korzhagin, N. V. Bulina, H. Kato, *Ceram. Int.* **2017**, *43*, 11902–11906.
- [34] F. Ding, A. Rosén, E. E. B. Campbell, L. K. L. Falk, K. Bolton, *J. Phys. Chem.* **2006**, *110*, 7666–7670.
- [35] P. Weisbecker, J.-M. Leyssale, *Techniques de l'Ingénieur* **2015**, NM3150, 1–25.
- [36] D. Balzar, *J. Res. Natl. Inst. Stand. Technol.* **1993**, *98*, 321.
- [37] R. E. Dinnebier, S. J. L. Billinge, Eds., *Powder Diffraction. Theory and Practice*, RSC Publishing, **2008**.
- [38] V. Uvarov, I. Popov, *Mater. Charact.* **2013**, *85*, 111–123.
- [39] J. Dugay, R. P. Tan, A. Loubat, L. M. Lacroix, J. Carrey, P. F. Fazzini, T. Blon, A. Mayoral, B. Chaudret, M. Respaud, *Langmuir* **2014**, *30*, 9028–9035.
- [40] M. Repoux, *Surface Interface Anal.* **1992**, *18*, 567–570.

---

Manuscript received: October 6, 2022

Revised manuscript received: November 1, 2022

Accepted manuscript online: November 6, 2022

Version of record online: December 30, 2022